

# Low-divergence femtosecond X-ray pulses from a passive plasma lens

Jonas Björklund Svensson<sup>1</sup>✉, Diego Guénot<sup>1</sup>, Julien Ferri<sup>2,3</sup>, Henrik Ekerfelt<sup>1,4</sup>, Isabel Gallardo González<sup>1</sup>, Anders Persson<sup>1</sup>, Kristoffer Svendsen<sup>1</sup>, László Veisz<sup>5</sup> and Olle Lundh<sup>1</sup>✉

**Electron and X-ray beams originating from compact laser-wakefield accelerators have very small source sizes that are typically on the micrometre scale. Therefore, the beam divergences are relatively high, which makes it difficult to preserve their high quality during transport to applications. To improve on this, tremendous efforts have been invested in controlling the divergence of the electron beams, but no mechanism for generating collimated X-ray beams has yet been demonstrated experimentally. Here we propose and realize a scheme where electron bunches undergoing focusing in a dense, passive plasma lens can emit X-ray pulses with divergences approaching the incoherent limit. Compared with conventional betatron emission, the divergence of this so-called plasma lens radiation is reduced by more than an order of magnitude in solid angle, while maintaining a similar number of emitted photons per electron. This X-ray source offers the possibility of producing brilliant and collimated few-femtosecond X-ray pulses for ultra-fast science, in particular for studies based on X-ray diffraction and absorption spectroscopy.**

Laser-wakefield accelerators<sup>1</sup> (LWFAs) have emerged over the past few decades as ultra-compact sources of high-energy (hundreds to thousands of megaelectronvolts), low-normalized-emittance (1 mm mrad)<sup>2</sup> and short-duration (few-femtosecond full-width at half-maximum (FWHM)<sup>3,4</sup>) electron bunches, as well as short and bright ( $10^{22}$  photons s<sup>-1</sup> 0.1% BW<sup>-1</sup> mrad<sup>-2</sup> mm<sup>-2</sup>; BW, bandwidth) femtosecond ‘betatron’ X-ray pulses<sup>5–8</sup>. LWFAs are normally operated in the bubble regime, where an ultra-intense ( $10^{18}$ – $10^{19}$  W cm<sup>-2</sup>) laser pulse drives a strongly nonlinear plasma wave by expelling the plasma electrons from a quasi-spherical region behind the laser, forming an ion cavity, or bubble. The electric fields in the bubble, which reach hundreds of gigavolts per metre, are directed radially away from its centre and have linear gradients, so as to both focus and accelerate the negatively charged electrons injected into the rear part of the bubble. Therefore, off-axis electrons will perform transverse oscillations as they accelerate, emitting X-rays in a forward-facing cone. Because of the strong focusing, the electron beams are typically transversely small (around 1  $\mu$ m FWHM), but their ensemble divergences are large (several milliradians FWHM) compared to conventional sources (tens of microradians). The X-ray divergence,  $\theta$ , is determined by the maximum excursion angle and energy of the electrons, quantified by the wiggler parameter,  $K$ , and the relativistic gamma factor,  $\gamma_b$ , as  $\theta = K/\gamma_b$ .  $K$  is often of the order of 10–20, yielding root-mean-square (r.m.s.) divergences in the tens of milliradians.

When considering applications of either beam, transportation and focusing greatly benefit from a reduction of this intrinsic divergence. For the electron beam, this not only lowers the requirements for downstream focusing elements, but also reduces, for example, free-space normalized emittance growth<sup>9</sup>. Much work has been done towards improving the transition between plasma and transport optics, such as plasma density tapering<sup>10–13</sup>, active (electric discharge) plasma lenses<sup>14,15</sup> and passive, laser-driven<sup>16,17</sup> and beam-driven<sup>18</sup> plasma lenses. For the X-ray beam, large incidence

angles on optics yield substantial photon absorption. One solution is to use mosaic crystals, but their implementation is cumbersome and they are prone to image distortion<sup>19</sup>. Although crucial, only theoretical schemes for lowering the intrinsic X-ray divergence have been proposed<sup>20,21</sup>; none have been practically demonstrated. In this Article, we experimentally show that electron bunches focused by a high-density, passive plasma lens can be used to emit X-ray beams with a significantly reduced divergence.

This compact and experimentally simple scheme is based on two points. First, the electron beam divergence at a waist or crest is inversely proportional to its size. Furthermore, the X-ray beam divergence depends on the divergence of the radiating electron beam, and thus also on the inverse electron beam size. Second, the focusing gradients inside a lower-density ( $10^{18}$  cm<sup>-3</sup> and below), linear laser-wake can be strong enough to collimate the electron beam<sup>16,17</sup>, but not strong enough to yield any meaningful X-ray emission. This changes quickly at higher plasma densities and/or when the plasma wave becomes nonlinear<sup>22,23</sup>. In this Article, the electrons are injected and accelerated in a primary stage and enter the wake excited in a secondary, higher-density stage, separated from the primary by a few millimetres (Fig. 1a). Therein, they are focused and radiate strongly due to the expanded beam envelope and strong focusing fields (Fig. 1a, inset), which reduces the X-ray divergence by at least a factor of 20 in solid angle compared to a reference ‘betatron wiggler’.

Reducing the divergence of X-ray beams makes them considerably more efficient to transport and lowers the cost associated with large reflective optics, considerably advancing their use for applications such as ultra-fast X-ray diffraction and absorption studies<sup>24</sup>. For example, the reflectivity of an iridium-coated mirror increases by an order of magnitude at 5 keV when the grazing incidence angle is reduced from 20 mrad to 5 mrad (ref. 25). The smaller divergence also reduces geometric aberrations from the optics, which, together with the increased photon collection and transport efficiency, could

<sup>1</sup>Department of Physics, Lund University, Lund, Sweden. <sup>2</sup>Department of Physics, Chalmers University of Technology, Gothenburg, Sweden. <sup>3</sup>Department of Physics, University of Gothenburg, Gothenburg, Sweden. <sup>4</sup>SLAC National Accelerator Laboratory, Menlo Park, CA, USA. <sup>5</sup>Department of Physics, Umeå University, Umeå, Sweden. ✉e-mail: jonas.bjorklund-svensson@desy.de; olle.lundh@fysik.lth.se

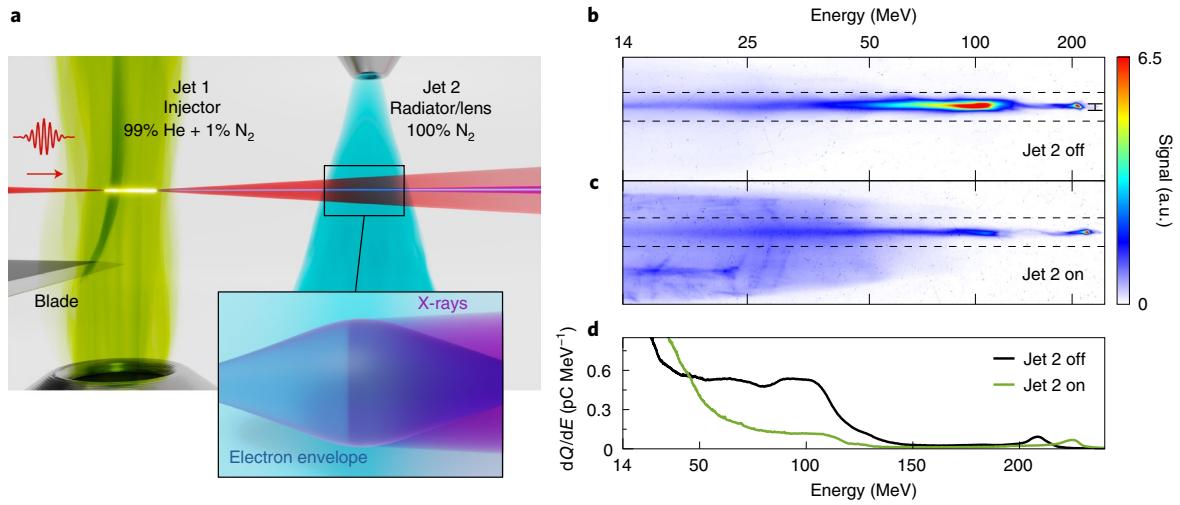


**Fig. 1 | Experimental set-up and electron beam examples.** **a**, Schematic of the experimental set-up, with the two gas jets and the razor blade. The inset conceptually shows the collimated X-rays being emitted as the electron beam envelope is strongly focused inside jet 2. **b,c**, Two example electron spectrometer scintillator images, with jet 2 off (**b**) and on (**c**). The black, vertical bar in **b** depicts 10 mrad divergence. **d**, Associated (on-axis) spectra within the dashed lines in **b** and **c**.

enable studies based on ultra-fast, compact X-ray diffraction, and greatly improve the signal-to-noise ratio in absorption spectroscopy. Furthermore, the quality of the radiating bunch deteriorates less than in a typical betatron radiation source, enabling further use of the bunch itself, for example in a tunable double-pulse source<sup>26</sup>. Through particle-in-cell (PIC) simulations and a semi-analytical model for electron-beam propagation, the electron-beam focusing and X-ray characteristics are reproduced, showing a path forward regarding tuning, optimization and upscaling of the scheme.

### Electron-beam generation and focusing

To generate the electron beams, shock-assisted ionization injection<sup>27</sup> is used in the first gas jet (jet 1) to inject two electron bunches in the same bubble. In this scheme, a gas mixture (Methods) is used in combination with a density shock-front to help localize the injection of the first electron bunch spatially<sup>28,29</sup>. To produce the shock-front, a razor blade is inserted into the upstream edge of the supersonic gas jet (Fig. 1a). The second bunch is continuously injected via ionization injection<sup>30</sup> as the laser propagates through the plasma. A typical electron spectrometer image with only jet 1 is shown in Fig. 1b, and its associated spectrum is shown by the black curve in Fig. 1d. The narrowband shock-front-injected electrons (the ‘shock-bunch’) are accelerated for a longer distance and thus reach higher energy, while the continuous injection in the plateau yields a broadband bunch at lower energies (the ‘ionization-bunch’). Typically, the shock-bunch has around 2 pC of charge, while the ionization-bunch has up to 100 pC. Figure 2a–c shows zoomed-in electron spectrometer images with only jet 1, and the associated spectra are shown in Fig. 2d.

When enabling the second jet (jet 2), two main effects can be observed on the electron beam (Figs. 1c,d and 2). First, the mean (vertical,  $y$ ) divergence of the ionization-bunch is greatly increased, from 8 to 47 mrad FWHM, while the mean divergence of the shock-bunch is decreased from 4.5 to 3 mrad FWHM. Also, the higher-energy end of the ionization-bunch, around 120 MeV, shows a reduction in divergence, which is in line with the fact that the laser-wake can also provide some focusing for the head of a bunch driving a wake<sup>22</sup>. Similar to ref. 17, a minimum of the shock-bunch divergence is found when scanning the jet separation, here at approximately 3 mm (from the jet 1 downramp half-max to the jet 2 centre), while the focusing effect is largely insensitive to the pressure in jet 2.

Second, the mean energy of the ionization-bunch decreases from 63 to 45 MeV (ref. 31), and a small, but statistically significant, mean energy gain from 206 to 219 MeV is observed for the shock-bunch (Fig. 2). This gain peaks at a jet separation of  $\sim 2$  mm, which is the smallest separation possible without visible gas flow collision. The energy gain increases slowly with the peak density in jet 2. The charge of the entire beam also increases by a few tens of picocoulombs, concentrated towards lower energies, with jet 2 on and predominantly at smaller jet separation. Additional electron spectrometer images are provided in Supplementary Fig. 3.

### Observation of low-divergence X-ray beams

In parallel with the effects on the electron beams, unusually low-divergence X-ray beams are also observed with jet 2 on. As shown in Fig. 3a, the X-ray beams emitted from jet 2 are collimated—typically around 4.5 to 5 mrad FWHM (around 2 mrad r.m.s.), compared to approximately 33 mrad FWHM horizontally ( $x$ ) and 14 mrad FWHM vertically ( $y$ ) for the X-rays emitted from jet 1 (Fig. 3b). In Fig. 3b, note that the density in jet 1 was increased by 15% to generate a measurable signal. In this way, the betatron radiation is enhanced by direct laser acceleration (DLA)<sup>32,33</sup>, where the transverse electron motion is enhanced by the laser fields. The narrow beams are observed in more than 95% of shots with the shock-bunch and jet 2 on. Divergence (Fig. 3c) is weakly dependent on the density in jet 2, but no effect is seen on the critical energy. No trend on divergence or critical energy with jet separation is observed. The integrated X-ray signal from jet 2 correlates well with the charge in the shock-bunch, as shown in Fig. 3d. Removing the shock blade, injecting only the ionization-bunch, leads to complete loss of the narrow radiation. The X-ray spectrum (Fig. 3e,f) is calculated using single-photon counting<sup>34</sup>. The number of photons and the critical energy are estimated to  $N_{ph} \lesssim 5 \times 10^6$  photons and  $E_c \approx 1.5$  keV, respectively, corresponding to a pulse energy of  $\sim 0.4$  nJ. Using the r.m.s. divergence half-axes, the emission solid angle is approximately  $14 \mu\text{sr}$  on average, which results in a yield of  $1 \times 10^8$  and  $9 \times 10^7$  ph  $0.1\% \text{BW}^{-1} \text{sr}^{-1}$  at 1 keV and 1.5 keV, respectively.

### Numerical investigations

To understand and confirm the behaviour observed in the experiment, PIC simulations were conducted using the code CALDER-Circ<sup>35</sup>. In these simulations, a 0.9-J, 35-fs laser pulse

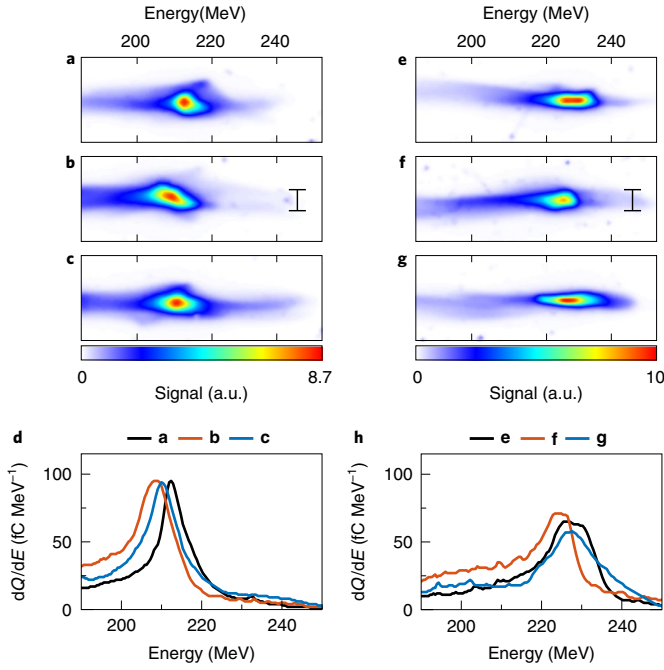


**Fig. 2 | Shock-bunch features.** **a–c**, Three example zoomed-in electron spectrometer images with jet 1 only. **d**, Associated spectra of the bunches in **a** (black), **b** (red) and **c** (blue). **e–g**, Three example zoomed-in electron spectrometer images with jet 2 on. Note the decrease in vertical size compared with **a–c**. **h**, Associated spectra of the bunches in **e** (black), **f** (red) and **g** (blue). The black bars in **b** and **f** depict 10 mrad divergence. Note that **b** and **f** correspond to Fig. 1b,c, respectively.

is focused at the entrance of the two-jet density profile shown in Fig. 4a (see Methods for further details). The evolution of the normalized vector potential,  $a_0$ , along the simulation shows self-focusing of the laser pulse in jet 1. Free-space diffraction between the jets lowers  $a_0$  to just above 0.5 at the entrance of jet 2, where it stays relatively constant and the laser is intense enough to ionize the gas and drive a linear wake.

After jet 2 (Fig. 4b,c), the shock-bunch divergence is decreased from 11.8 to 6.6 mrad and 5.1 to 3.4 mrad r.m.s. in the  $x$  (horizontal, parallel with the laser polarization) and  $y$  (vertical) directions, respectively. Conversely, the divergence of the ionization-bunch (not shown) slightly increases from 17.1 to 20.4 mrad r.m.s. in the  $x$  direction and more than doubles in the  $y$  direction (from 9.1 to 19.0 mrad r.m.s.). The larger divergence in the  $x$  direction is due to DLA, with angular peaks seen off-axis for the shock-bunch (Fig. 4b,e), and both beams show some temporal modulation (Fig. 4f). The difference in behaviour of the shock- and ionization-bunches corresponds to the respective distribution of these two components in the wake generated in jet 2 (Fig. 4g,h). The front of the electron beam, containing higher electron energies, sees accelerating and focusing fields, while the lower-energy electrons at the less localized back overlap with defocusing and decelerating parts in the combined laser- and beam-driven wake.

Finally, the X-ray emission was computed by post-processing a representative sample of electron trajectories from the PIC simulations (Methods). Figure 4d shows the divergence in the  $y$  direction of the X-ray emission from jet 1 (black line) and jet 2 (green line), showing a decrease from 6.3 mrad to 2.0 mrad FWHM for photon energies above 3 keV, similar to what was observed in the experiment. The radiated spectrum is synchrotron-like with a critical energy of 0.8 keV and  $2.1 \times 10^7$  photons.

The interaction between the laser pulse, electron bunches and the plasma is similar to the case studied in ref. 22. The moderately intense laser pulse drives a linear wake in jet 2, inside which the dense electron beam drives a higher-amplitude, nonlinear wake. To gain additional understanding of the electron beam focusing and X-ray generation, a semi-analytical model of the propagation of the electron beam envelope,  $\beta(s)$  (Methods), is constructed. Using the force on an electron in a laser- and beam-driven wake<sup>22</sup>, the equation<sup>36</sup>

$$\frac{1}{2}\beta'' + \kappa(s)\beta - \frac{1}{\beta} \left[ 1 + \left( \frac{1}{2}\beta' \right)^2 \right] = 0 \quad (1)$$

is solved numerically. Here,  $\kappa(s)$  is the normalized focusing strength of the wake at longitudinal position  $s$ . The ionization-bunch is assumed to dominate the excitation of the second wake and the shock-bunch samples the fields generated therein. Details are provided in the Methods and Supplementary Information.

As observed in the experiment, the model replicates a minimum in shock-bunch divergence when changing the jet separation (Fig. 5a). The focusing gradients experienced by the two bunches as they propagate through the varying plasma density (Fig. 5b) cause the bunch envelopes to change, as shown in Fig. 5c. Note that the shock-bunch divergence has a minimum at the maximum of the bunch radius. Like the PIC simulations, this model yields that the shock-bunch is located towards the front of the ionization-bunch. Figure 5d shows the radiated power calculated from the beam envelope and focusing gradient shown in Fig. 5c,b (Methods). The radiated power has a maximum around where the electron divergence has its minimum, yielding radiation with an estimated effective divergence of approximately 2.8 mrad FWHM (1.2 mrad r.m.s.), a critical energy of 0.3 keV and a photon yield of  $5 \times 10^5$  photons.

## Accuracy and interpretation of the numerical results

The vertical shock-bunch focusing shown in Fig. 2a–c,e–g is consistent, as can also be seen in Fig. 5a; almost all configurations with jet 2 on yield a smaller divergence than with only jet 1. The growth of low-energy electron divergence decreases with jet separation, which is consistent with the beam-induced wake amplitude decreasing because of lower driver beam density<sup>31</sup>. The PIC simulations generally reproduce the experimental results, showing an electron energy gain slightly above 10 MeV and focusing for the shock-bunch in jet 2, with reduced X-ray divergence and modest photon energy. The simulations show that the shock-bunch is located towards the front of the ionization-bunch, sitting in a weak beam-driven wake. The modelled beam-driven wake is also relatively weak, but assists in the shock-beam focusing. The additional charge that is experimentally observed with jet 2 on appears to come from low-energy electrons that are injected in the downramp of jet 1 and subsequently accelerated in the beam-driven wake in jet 2, to energies above the lower spectrometer cutoff.

The experimental and modelled electron divergences agree when accounting for the imaging system resolution, and only the total radiated and critical X-ray energies (and thus average photon number and energy) differ. This is attributed to the model not accounting for the relative bunch–laser or bunch–bunch movement, electron beam self-focusing and the lack of horizontal divergence data (which is here approximated using the vertical data), for example. The model also assumes transversely Gaussian distributions, which, as seen in Fig. 4b, might not be the case, and the large off-axis electron population caused by DLA could enhance the X-ray emission. The model predicts effective X-ray divergences (Methods) of 1.2 and 6.2 mrad r.m.s. ( $y$ ) for the shock-bunch with jet 2 on and ionization-bunch with jet 2 off, respectively, which



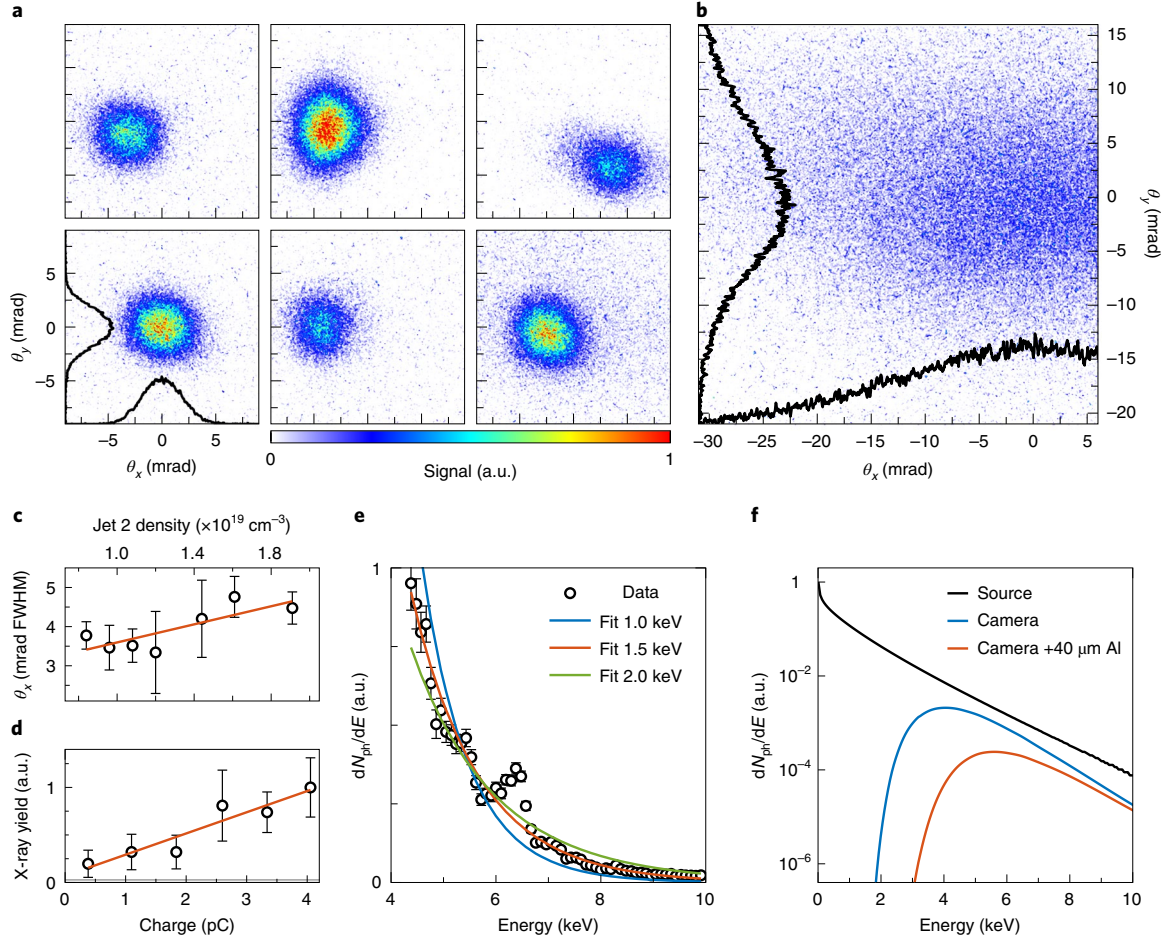


**Fig. 3 | X-ray emission from jet 2.** **a**, X-ray profiles from six consecutive shots when jet 2 is on. **b**, X-ray profile when jet 2 is off. Note that the pressure in jet 1 was increased to generate a measurable signal, and that this divergence is smaller than that of a more optimized (for photon number) betatron source with similar laser parameters<sup>37</sup>. **c**, Divergence as a function of jet 2 peak plasma density. Error bars show the r.m.s. fluctuations. The orange line shows a linear fit to the data. **d**, Integrated X-ray signal from jet 2 as a function of the total charge above 140 MeV. Error bars show the r.m.s. fluctuations. The grey line at the bottom shows the noise level from the jet 1 signal and the orange line shows a linear fit to the data. **e**, Renormalized, averaged X-ray spectrum ( $dN_{\text{ph}}/dE$ ) at the source as measured using single-photon counting, fit with synchrotron spectra of critical energy 1.0, 1.5 and 2.0 keV. The large spike at 6.4 keV comes from the iron  $K\alpha$  line, and is not part of the source emission spectrum. Error bars show the r.m.s. fluctuations. **f**, The 1.5 keV X-ray spectrum at the source compared with the signal on the camera, after filter transmission and sensor response. The blue curve shows the response used for **a** and **b** and the other profile measurements, and the orange line shows the response for the single-photon counting measurements, which includes an additional 40  $\mu\text{m}$  aluminium filter to decrease the X-ray flux.

are close to the experimental minima of 1.6/1.6 ( $x/y$ ) and 6.8 mrad r.m.s. ( $y$ ), respectively (cf. Fig. 3).

All combinations of model parameters yielding a qualitative agreement in electron divergence with the experiment—optimal collimation surrounded by regions of over-collimation (small  $\Delta s$ ) and under-collimation (large  $\Delta s$ ) (Fig. 5a)—show a maximum in radiated power around regions of small electron beam divergence. This is a general feature of the source—as long as the focusing gradient is sufficiently high, here  $g_{\text{f}} > 1 \text{ MT m}^{-1}$  ( $\kappa \approx 1.4 \times 10^6 \text{ m}^{-2}$ ), the change in transverse momentum will be maximal at or near the envelope crest, thus coinciding with the smallest electron beam divergence. This brings the X-ray divergence substantially closer to the incoherent r.m.s. limit  $\sigma_{\theta} = 1/(1.95\gamma_b)$  (Supplementary Table 1 and Supplementary Fig. 4). The larger the on-crest envelope of the electron beam, the smaller its contribution to the X-ray beam divergence will be. During ‘conventional’ betatron radiation emission, the electrons of the bunch perform individual, asynchronous transverse oscillations as they accelerate in the forward direction<sup>8</sup>, while their collective envelope is relatively constant. By contrast,

the collimated X-ray emission from our source occurs during a fraction of a betatron oscillation, and the correlation between the electrons’ propagation angle and position that builds up in the space between the two jets causes their trajectories to be more synchronized and similar to the envelope shape. Because of this discrepancy in phenomenology, we term this novel radiation ‘plasma-lens radiation’ (PLR).

### Comparison to conventional betatron radiation

A conventional betatron source using similar laser parameters<sup>37,38</sup> has a similar X-ray angular yield, at approximately  $5 \times 10^7 \text{ ph } 0.1\% \text{ BW}^{-1} \text{ sr}^{-1}$  at 1 keV (compared to  $1 \times 10^8 \text{ ph } 0.1\% \text{ BW}^{-1} \text{ sr}^{-1}$  here), but with two orders of magnitude higher radiating charge. Using 2 pC of charge (average, cf. Fig. 3d) and  $5 \times 10^6$  photons, as measured in this study, the photon yield corresponds to 0.4 photons per electron—similar to what one would expect from a betatron source<sup>8,39</sup>, but with a notably smaller opening angle. Assuming a pulse duration of 5 fs FWHM (equal to the shock-bunch duration in the PIC simulations,

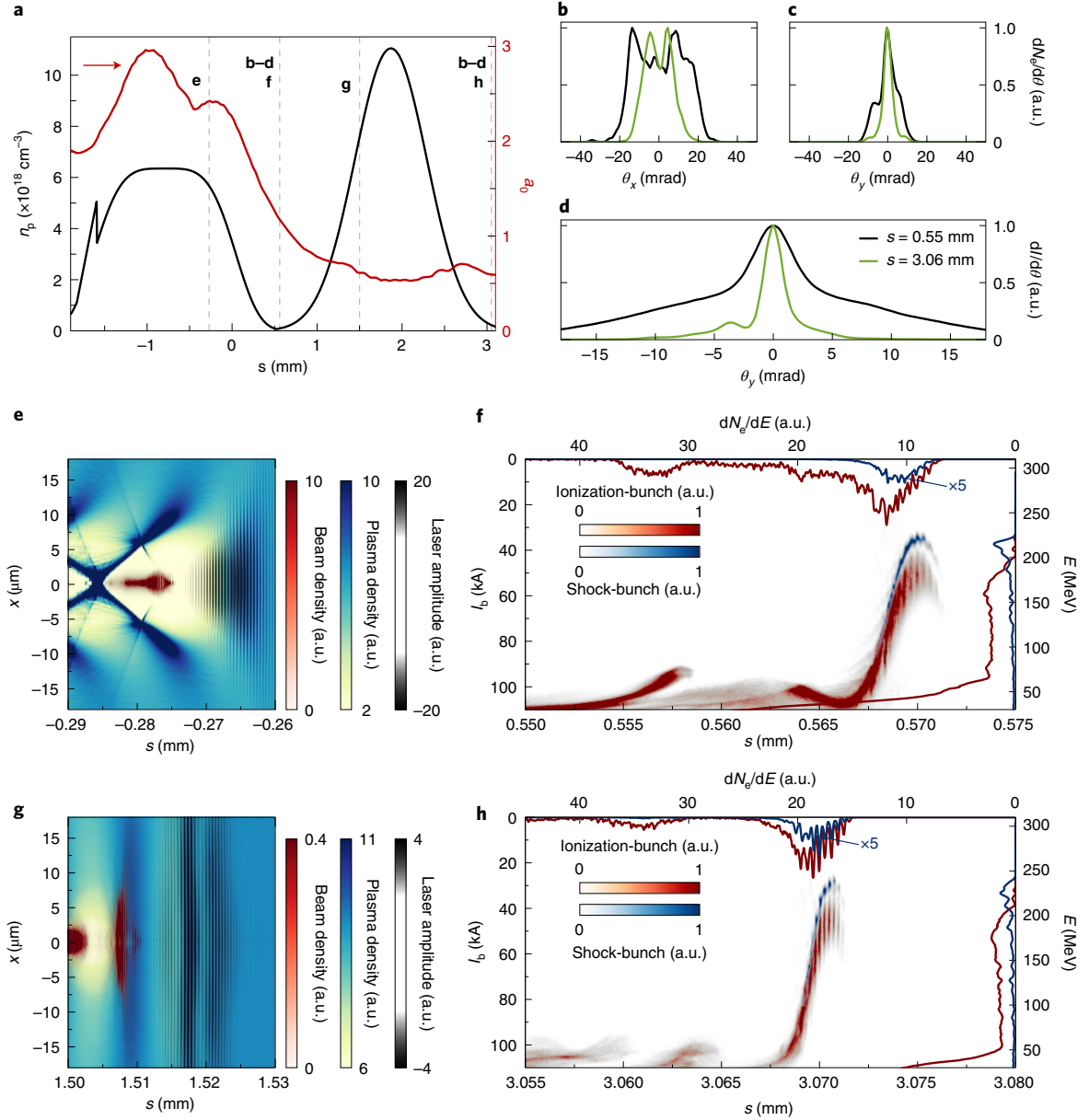


**Fig. 4 | PIC simulation results.** **a**, Plasma density profile used in the simulations ( $n_p$ , black) and normalized vector potential ( $a_0$ , red) along propagation with longitudinal coordinate  $s$ . The propagation direction is given by the red arrow.  $s=0$  corresponds to the downstream half-max of the jet 1 density distribution, such that the jet separation,  $\Delta s$ , is defined as the difference from the jet 1 half-max to the jet 2 centre. The vertical dashed lines show the locations of the respective sub-figures. **b,c**, Shock-electron angular distributions ( $dN_e/d\theta$ ) at 0.55 mm (black, exit of jet 1) and 3.06 mm (green, exit of jet 2) along  $x$  (**b**) and  $y$  (**c**). **d**, Vertical ( $y$ ) X-ray angular intensity distribution ( $dI/d\theta$ ) from jet 1 (black) and jet 2 (green), that is, corresponding, respectively, to propagation between  $-2$  and  $0.55$  mm and between  $0.55$  mm and  $3.06$  mm, for photon energies of  $3$ – $15$  keV. **e**, Cross-section of the laser-plasma interaction showing the plasma (yellow-blue) and beam (red) electron densities, and laser amplitude (black), at the end of the jet 1 plateau. **f**, Longitudinal phase space after jet 1, displaying also the current ( $I_b$ ) and spectrum ( $dN_e/dE$ ) of the shock- and ionization-bunch distributions projected onto their corresponding axes. The shock-bunch current has been increased by a factor of 5 for visibility. **g**, Cross-section of the laser-plasma interaction in the density up-ramp of jet 2, with the same conventions as in **e**. Note that the leftmost electron distribution ( $s=1.50$  mm) corresponds to the leftmost distribution in **f** ( $s=0.555$  mm), and consists of electrons injected in the downramp at the end of jet 1. **h**, Longitudinal phase space after jet 2, with the same conventions as in **f**.

Fig. 4f,h) and a source size of  $2\text{ }\mu\text{m}$  r.m.s., the estimated brilliance at  $1\text{ keV}$  is then on the order of  $10^{21}\text{ ph s}^{-1}0.1\%\text{BW}^{-1}\text{ mm}^{-2}\text{ mrad}^{-2}$ . The reasons that the radiation from the ionization-bunch is not observed are that it radiates with a larger divergence ( $\theta \propto 1/\gamma_b$ ) and with a lower photon energy ( $E_c \propto \gamma_b^2$ ), yielding low angular flux and high absorption in the vacuum windows (Fig. 3b,f and Supplementary Fig. 2).

The PLR wiggler  $K$  parameter can be inferred from the measured critical energy,  $E_c$ , and electron energy,  $\gamma_b$ , as  $K = E_c \lambda_\beta / (3\pi \gamma_b^2 \hbar c) \approx 9$  (ref. <sup>8</sup>), where  $\lambda_\beta$  is the betatron wavelength (Methods). This  $K$  yields  $1.9 \times 10^6$  emitted photons and is close to what is normally measured for laser-wakefield accelerators, but is in this case inconsistent with the X-ray divergence (usually given by  $\theta = K/\gamma_b$ ) as the electrons only perform a partial betatron oscillation and never reach their

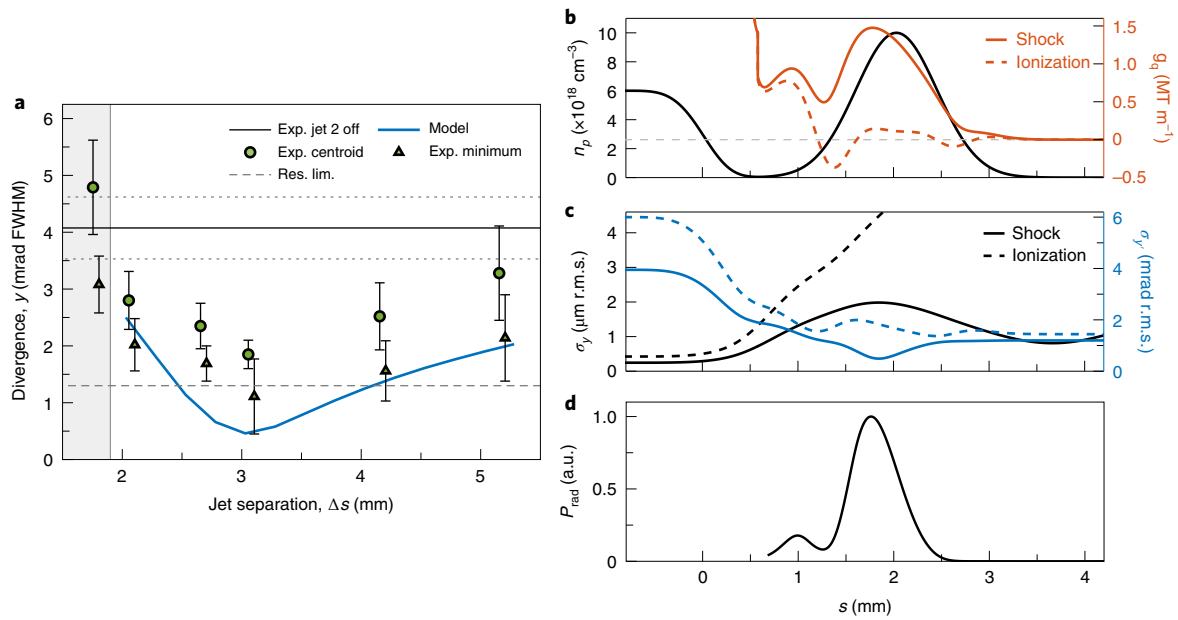


**Fig. 5 | Results from the semi-analytical model. a,** Experimental FWHM divergences of the shock-bunch as a function of jet separation,  $\Delta s$ , with error bars and dotted lines denoting r.m.s. fluctuations. The experimental divergences are de-convoluted with the optical resolution of the spectrometer imaging system (Methods). The black line shows the reference value with jet 2 off, green triangles show the minimum (slice) divergence on the spectrometer, green circles show the centroid divergence (Methods), the solid blue line shows the prediction from the semi-analytical model and the dashed grey line shows the corresponding FWHM optical resolution of the imaging system. The grey area shows where gas flow collisions were visible on the lateral probe, at  $\Delta s \leq 1.75$  mm separation. **b,** Plasma electron density ( $n_p$ , black) and resulting focusing gradients ( $g_q$ , red) experienced by the shock- (solid) and ionization-bunches (dashed) in the model during propagation. The dashed grey line shows  $g_q = 0$  ( $g_q < 0$  is defocusing). **c,** R.m.s. beam size ( $\sigma_r$ , black) and divergence ( $\sigma_y$ , blue) of the shock- (solid) and ionization-bunches (dashed) during propagation through the focusing gradient in **b**. **d,** Average radiated power ( $P_{\text{rad}}$ ) in jet 2 calculated from equation (3) in the Methods using the focusing gradient in **b** and beam size in **c**. The peak power overlaps with regions of low electron-beam divergence.

maximum propagation angle. This suggests that  $K$  is not a useful figure of merit for this type of source.

### Scalability and applications

Because of the increasing wakefields towards the back of the driving ionization-bunch, focusing gradients greater than  $1 \text{ MT m}^{-1}$  can also be achieved at lower plasma densities in a two-bunch scheme, if the bunches can be separated longitudinally. The scheme is expected to work for single bunches in pure laser-wakefields, as long as a high enough wake amplitude can be reached. This would be possible at higher-power ( $P \gtrsim 100 \text{ TW}$ ) laser facilities where the laser Rayleigh length is typically longer ( $s_R \gtrsim 1 \text{ mm}$ ), limiting diffraction between adjacent stages. These lasers are also expected to yield higher electron energies (above  $200 \text{ MeV}$ ) and much higher bunch charges of several hundred picocoulombs<sup>40–42</sup>, and thus have the potential to increase the X-ray yield by several orders of magnitude to beyond  $10^9$  photons. Such high-charge bunches would also drive very strong self-wakes, which would further enhance the X-ray yield. Theoretical schemes using dual-stage plasma configurations have been suggested as a method for high-brilliance  $\gamma$ -ray generation<sup>23,43</sup>, but these do not yield collimated photon beams because of the small electron beam size. Based on the higher charge alone, the PLR brilliance could reach above  $10^{23} \text{ ph s}^{-1} 0.1\% \text{ BW}^{-1} \text{ mm}^{-2} \text{ mrad}^{-2}$  and if the electron beam is expanded sufficiently (Methods),  $\gamma_b \gtrsim 850$  could yield sub-1-mrad FWHM X-ray divergence. The increased brilliance and reduced divergence can allow for the use of monochromators, potentially enabling hitherto unfeasible applications for laser-wakefield generated X-rays such as ultra-fast X-ray diffraction, as the expected photon numbers from high-charge sources after the monochromator exceed the required values<sup>44</sup>. Because the shock-bunch quality appears to be preserved, one could also envision

using the radiating bunch for further applications, for example with inverse Compton scattering (ICS) for a two-colour X-ray source in a compact, tunable PLR + ICS multi-pulse configuration<sup>26</sup>.

This technique could also lend itself to electron beam focusing in high-energy experiments and/or hybrid-wakefield<sup>41,45</sup> and LWFA staging schemes. Applying a ‘driver-witness’ configuration where the bunches are longitudinally separated, one can drive a nonlinear or blown-out wakefield in which the focusing forces on the witness are much stronger. A similar scheme was recently studied theoretically in ref. <sup>18</sup> for 10-GeV beams at FACET-II<sup>46</sup>, energies that some LWFA experiments are also approaching<sup>47</sup>. In hybrid-wakefield schemes, the witness bunch can be focused more strongly in the nonlinear than in the linear wake, simplifying matching into the second acceleration stage. This, in combination with the driver bunch collimation, possibly increases the maximum acceleration distance. However, synchrotron radiation already presents a problem for particle colliders using conventional focusing technologies, and so the radiation from this type of lens must be considered for sensitive applications, for example future plasma-based colliders or coherent X-ray sources.

Received: 7 July 2020; Accepted: 17 December 2020;  
Published: xx xx xxxx

## References

1. Tajima, T. & Dawson, J. M. Laser electron accelerator. *Phys. Rev. Lett.* **43**, 267–270 (1979).
2. Barber, S. K. et al. Measured emittance dependence on the injection method in laser plasma accelerators. *Phys. Rev. Lett.* **119**, 104801 (2017).
3. Lundh, O. et al. Few femtosecond, few kiloampere electron bunch produced by a laser-plasma accelerator. *Nat. Phys.* **7**, 219–222 (2011).
4. Buck, A. et al. Real-time observation of laser-driven electron acceleration. *Nat. Phys.* **7**, 543–548 (2011).
5. Phuoc, K. T. et al. Imaging electron trajectories in a laser-wakefield cavity using betatron X-ray radiation. *Phys. Rev. Lett.* **97**, 225002 (2006).
6. Albert, F. et al. Betatron oscillations of electrons accelerated in laser wakefields characterized by spectral X-ray analysis. *Phys. Rev. E* **77**, 056402 (2008).
7. Kneip, S. et al. Bright spatially coherent synchrotron X-rays from a table-top source. *Nat. Phys.* **6**, 980–983 (2010).
8. Corde, S. et al. Femtosecond X-rays from laser-plasma accelerators. *Rev. Mod. Phys.* **85**, 1–48 (2013).
9. Migliorati, M. et al. Intrinsic normalized emittance growth in laser-driven electron accelerators. *Phys. Rev. ST Accel. Beams* **16**, 011302 (2013).
10. Floetmann, K. Adiabatic matching section for plasma accelerated beams. *Phys. Rev. ST Accel. Beams* **17**, 054402 (2014).
11. Xu, X. L. et al. Physics of phase space matching for staging plasma and traditional accelerator components using longitudinally tailored plasma profiles. *Phys. Rev. Lett.* **116**, 124801 (2016).
12. Ariniello, R., Doss, C. E., Hunt-Stone, K., Cary, J. R. & Litos, M. D. Transverse beam dynamics in a plasma density ramp. *Phys. Rev. Accel. Beams* **22**, 041304 (2019).
13. Zhao, Y. et al. Emittance preservation through density ramp matching sections in a plasma wakefield accelerator. *Phys. Rev. Accel. Beams* **23**, 011302 (2020).
14. van Tilborg, J. et al. Active plasma lensing for relativistic laser-plasma-accelerated electron beams. *Phys. Rev. Lett.* **115**, 184802 (2015).
15. Lindström, C. A. et al. Emittance preservation in an aberration-free active plasma lens. *Phys. Rev. Lett.* **121**, 194801 (2018).
16. Lehe, R., Thaur, C., Guillaume, E., Lifschitz, A. & Malka, V. Laser-plasma lens for laser-wakefield accelerators. *Phys. Rev. ST Accel. Beams* **17**, 121301 (2014).
17. Thaur, C. et al. Demonstration of relativistic electron beam focusing by a laser-plasma lens. *Nat. Commun.* **6**, 6860 (2015).
18. Doss, C. E. et al. Laser-ionized, beam-driven, underdense, passive thin plasma lens. *Phys. Rev. Accel. Beams* **22**, 111001 (2019).
19. Šmíd, M. et al. Highly efficient angularly resolving X-ray spectrometer optimized for absorption measurements with collimated sources. *Rev. Sci. Instrum.* **88**, 063102 (2017).
20. Rykovanov, S. G., Schroeder, C. B., Esarey, E., Geddes, C. G. R. & Leemans, W. P. Plasma undulator based on laser excitation of wakefields in a plasma channel. *Phys. Rev. Lett.* **114**, 145003 (2015).
21. Xiao, H. et al. Control of transverse motion and X-ray emission of electrons accelerated in laser-driven wakefields by tuning laser spatial chirp. *Plasma Phys. Control. Fusion* **62**, 024002 (2019).
22. Lehe, R., Thaur, C., Lifschitz, A., Rax, J.-M. & Malka, V. Transverse dynamics of an intense electron bunch traveling through a pre-ionized plasma. *Phys. Plasmas* **21**, 043104 (2014).
23. Ferri, J. et al. High-brilliance betatron  $\gamma$ -ray source powered by laser-accelerated electrons. *Phys. Rev. Lett.* **120**, 254802 (2018).
24. Mahieu, B. et al. Probing warm dense matter using femtosecond X-ray absorption spectroscopy with a laser-produced betatron source. *Nat. Commun.* **9**, 3276 (2018).
25. Thick mirror reflectivity tool (Center for X-ray Optics, LBNL); [https://henke.lbl.gov/optical\\_constants/](https://henke.lbl.gov/optical_constants/)
26. Wenz, J. et al. Dual-energy electron beams from a compact laser-driven accelerator. *Nat. Photon.* **13**, 263–269 (2019).
27. Thaur, C. et al. Shock assisted ionization injection in laser-plasma accelerators. *Sci. Rep.* **5**, 16310 (2015).
28. Schmid, K. et al. Density-transition based electron injector for laser driven wakefield accelerators. *Phys. Rev. ST Accel. Beams* **13**, 091301 (2010).
29. Buck, A. et al. Shock-front injector for high-quality laser-plasma acceleration. *Phys. Rev. Lett.* **110**, 185006 (2013).
30. McGuffey, C. et al. Ionization induced trapping in a laser wakefield accelerator. *Phys. Rev. Lett.* **104**, 025004 (2010).
31. Chou, S. et al. Collective deceleration of laser-driven electron bunches. *Phys. Rev. Lett.* **117**, 144801 (2016).
32. Shaw, J. L. et al. Role of direct laser acceleration of electrons in a laser wakefield accelerator with ionization injection. *Phys. Rev. Lett.* **118**, 064801 (2017).
33. GallardoGonzález, I. et al. Effects of the dopant concentration in laser wakefield and direct laser acceleration of electrons. *New J. Phys.* **20**, 053011 (2018).
34. Fourment, C. et al. Broadband, high dynamics and high resolution charge coupled device-based spectrometer in dynamic mode for multi-keV repetitive X-ray sources. *Rev. Sci. Instrum.* **80**, 083505 (2009).
35. Lifschitz, A. F. et al. Particle-in-cell modelling of laser-plasma interaction using Fourier decomposition. *J. Comput. Phys.* **228**, 1803–1814 (2009).
36. Lee, S. Y. *Accelerator Physics* 3rd edn (World Scientific, 2011).
37. Svendsen, K. et al. Optimization of soft X-ray phase-contrast tomography using a laser wakefield accelerator. *Opt. Express* **26**, 33930–33941 (2018).
38. Gallardo Gonzalez, I. *Development and Applications of a Laser-Wakefield X-ray Source*. PhD thesis, Lund Univ. (2019).
39. Albert, F. & Thomas, A. G. R. Applications of laser wakefield accelerator-based light sources. *Plasma Phys. Control. Fusion* **58**, 103001 (2016).
40. Couperus, J. P. et al. Demonstration of a beam loaded nanocoulomb-class laser wakefield accelerator. *Nat. Commun.* **8**, 487 (2017).
41. Gilljohann, M. F. et al. Direct observation of plasma waves and dynamics induced by laser-accelerated electron beams. *Phys. Rev. X* **9**, 011046 (2019).
42. Götzfried, J. et al. Physics of high-charge electron beams in laser-plasma wakefields. *Phys. Rev. X* **10**, 041015 (2020).
43. Zhu, X.-L. et al. Extremely brilliant GeV  $\gamma$ -rays from a two-stage laser-plasma accelerator. *Sci. Adv.* **6**, eaaz7240 (2020).
44. Wang, X. et al. Role of thermal equilibrium dynamics in atomic motion during nonthermal laser-induced melting. *Phys. Rev. Lett.* **124**, 105701 (2020).
45. Hidding, B. et al. Monoenergetic energy doubling in a hybrid laser-plasma wakefield accelerator. *Phys. Rev. Lett.* **104**, 195002 (2010).
46. Yakimenko, V. et al. FACET-II facility for advanced accelerator experimental tests. *Phys. Rev. Accel. Beams* **22**, 101301 (2019).
47. Gonsalves, A. J. et al. Petawatt laser guiding and electron beam acceleration to 8 GeV in a laser-heated capillary discharge waveguide. *Phys. Rev. Lett.* **122**, 084801 (2019).

**Publisher's note** Springer Nature remains neutral with regard to jurisdictional claims in published maps and institutional affiliations.

© The Author(s), under exclusive licence to Springer Nature Limited 2021



## Methods

**Laser system.** The experiment was carried out at the Lund Laser Centre, in the high-intensity arm of the Lund Multi-Terawatt Laser, a Ti:sapphire system with a central wavelength at 800 nm, running at 10 Hz, delivering 34 fs FWHM pulses with  $\geq 800$  mJ on target. A 14.3° off-axis parabolic mirror (OAP) with  $f = 775$  mm ( $f/13$ ) was used to focus the laser pulses to a vacuum focal spot size of  $\sim 13 \times 13$   $\mu\text{m}$  FWHM, for an estimated  $a_0$  of 2.1–2.3 and Rayleigh length of 0.48 mm. A wavefront sensor (Phasics SID4), located downstream of the OAP, was connected in a closed loop with a deformable mirror to optimize the wavefront at the location of the deformable mirror. Frequency-resolved optical gating was used for the pulse duration measurements. A small pickup mirror at 45° was inserted into the edge of the laser beam before the OAP and used for transverse imaging of the laser–plasma interaction. Supplementary Fig. 1 presents a schematic of the experimental set-up.

**Gas jets.** The primary jet (jet 1) was a 1.5-mm-diameter supersonic de Laval gas nozzle, operated by a fast solenoid valve and fed by a 99% He + 1% N<sub>2</sub> gas mixture. The nozzle was positioned 2 mm below the laser axis. A razor blade on a piezo-actuator stage was inserted into the gas flow from the laser upstream direction, 1 mm above the nozzle. The secondary jet (jet 2) was a 400- $\mu\text{m}$ -diameter subsonic needle, fed with pure N<sub>2</sub> and placed at a variable distance of 1–10 mm from jet 1 in the laser downstream direction, at a distance of 1 mm from the laser axis. Both jets were characterized offline using the Phasics SID4 wavefront sensor, with and without the razor blade. The density distribution of jet 1 was a roughly fourth-order super-Gaussian of 1.6 mm FWHM (850  $\mu\text{m}$  plateau and 750  $\mu\text{m}$  ramps) and jet 2 was a Gaussian of 1 mm FWHM (Fig. 4a). A jet 1 plateau plasma electron density around  $6 \times 10^{18} \text{ cm}^{-3}$  yielded the best characteristics for the electron beams in terms of divergence, charge and energy. The shock-front was created in the density up-ramp of jet 1 and was positioned close to the laser focal plane by moving the entire jet assembly. The shock at this location could not be properly resolved in the gas density measurements, but was estimated (using the Mach number and shock-front angle<sup>38,40</sup>) to be 45% above the non-shock density at the blade location, yielding a peak shock-front density of  $\sim 5 \times 10^{18} \text{ cm}^{-3}$ .

**LWFA stage.** The LWFA stage (jet 1) was operated using a combination of ionization injection<sup>30</sup> and shock-front injection<sup>28,29</sup>, but not quite in the same conditions as previously shown shock-assisted ionization injection<sup>27</sup>, as both a quasi-monoenergetic peak and a continuous spectrum were obtained here. The shock is essential to the injection process, because the quasi-monoenergetic features are not observed without the blade.

Shock-front injection causes localized wavebreaking and injects electrons from the back of the bubble by rapidly increasing the bubble size, while ionization injection releases electrons near the laser intensity peak (in the first half of the bubble), which drift backward before being trapped. In shock-assisted ionization injection, however, the electrons that are trapped are ionization-injected electrons from around the shock-front density peak. The pure shock-front injected electrons are lost due to the local minimum in density between the shock and plateau, because they are injected at the back of the bubble, which retracts again when the density increases towards the plateau, while the trapping conditions for some fraction of the ionized, nitrogen-derived electrons are favourable.

**Electron spectrometer.** After acceleration, the electrons were deflected by a 0.83-T, 203-mm (8-in) permanent dipole magnet onto a Lanex Regular scintillating screen imaged by an Andor Zyla 16-bit scientific complementary metal–oxide–semiconductor (sCMOS) camera. The magnetic field of the dipole magnet was mapped using a Hall probe (Hirst GM08) and the electron trajectories were numerically tracked in the experimental geometry using the obtained field map to yield the dispersion curve on the scintillator screen. The imaging set-up was intensity-calibrated using a 532-nm diode laser (Thorlabs DJ532-10) (near the peak emission wavelength of the Lanex screen of 546 nm) with measured average power, together with a fast shutter with measured opening time and the Lanex emission data provided in ref. <sup>49</sup>, to provide an absolute value of the electron beam charge.

The dispersion plane of the dipole magnet is horizontal, parallel to the vacuum chamber floor and the laser polarization. As the electrons propagate freely (neglecting magnetic edge-field effects in the magnet) in the vertical direction, knowing the length of the electron trajectories from the numerical tracking allows for an estimate of the electron beam divergence in the vertical direction. A complete three-dimensional mapping of the magnetic field was not done, so any vertical edge effects are not taken into account. However, these edge effects are expected to be small.

The minimum measurable divergence is limited by the optical resolution of the imaging system and the scintillating screen. The intensity at a sharp, opaque edge (the edge response<sup>50</sup>) drops from 90% to 10% in about 3.62 pixels for an error function fit, and differentiating the fit yields a Gaussian (line spread) function with a standard deviation 1.41 pixels. The camera pixel size and spectrometer geometry yield 0.4 mrad px<sup>−1</sup> at 210 MeV (that is, 2-mrad divergence yields a size of 5.3 pixels), giving a resolution of  $1.41 \times 0.4 \approx 0.56$  mrad r.m.s. (1.3 mrad FWHM). When adding the resolutions in quadrature (that is, assuming two Gaussian distributions), an electron beam with divergence of 0.5 mrad FWHM would then

appear as having a divergence of 1.4 mrad FWHM. The minimum spatial extent of a point-like scintillation signal was not quantified.

**X-ray detection.** An Andor Ikon-L SO back-illuminated deep-depletion X-ray charge-coupled device (CCD) camera was used to detect the X-rays. This has  $2,048 \times 2,048$  pixels of 13.5  $\mu\text{m}$  cooled to  $-70^\circ\text{C}$ . Before hitting the CCD chip, the X-rays traversed a 3  $\mu\text{m}$  aluminium laser blocking foil, a 50  $\mu\text{m}$  kapton window and a 250  $\mu\text{m}$  Be window, and 1 cm in air. The camera was placed 75 cm from the source.

The X-ray spectrum was determined using the single-photon counting technique<sup>51</sup>. To reduce the X-ray flux sufficiently, the camera was placed further away from the source (1.6 m) and a 40  $\mu\text{m}$  Al foil was added. In this way, a photon per pixel ratio below 1% was achieved. Only single- and dual-pixel events were taken into account for this measurement because they allow for a more reliable estimation of the spectrum. Once the spectrum at the detector was acquired, it was renormalized by taking into account the transmission of all the absorbing elements in the transport line as well as the detector's quantum efficiency to get the spectrum at the source. To obtain the critical energy, the spectrum was fitted with the function<sup>51</sup>

$$\frac{\partial^2 N_{\text{ph}}}{\partial E \partial \Omega} \propto \xi(1 + \gamma_b^2 \theta^2)^{1/2} \left[ \frac{\gamma_b^2 \theta^2}{1 + \gamma_b^2 \theta^2} K_{1/3}^2(\xi) + K_{2/3}^2(\xi) \right],$$

where  $\gamma_b$  is the electron Lorentz factor,  $K_{1/3}$  and  $K_{2/3}$  the modified Bessel functions,  $\theta$  the observation angle with respect to the electron bunch propagation axis,  $E$  the photon energy,  $E_c$  the critical energy and  $\xi = \frac{E}{2E_c} (1 + \gamma_b^2 \theta^2)^{3/2}$ .  $E_c$  is the only relevant parameter for the calibration because it determines the 'shape' of the spectrum, while the other parameters determine the total number of photons. Given that the X-ray beam is contained within a relatively small solid angle, this equation is integrated between  $\gamma_b \theta = 0$  and 1 before fitting.

Once the critical energy is obtained, it is then used to estimate the fraction of photons that reach the detector and thus to determine the X-ray flux at the source. Note that, because of the strong absorption below 4.5 keV, only the part of the spectrum above this energy is included in the fit. Supplementary Fig. 2 presents X-ray transmission curves.

$E_c$  can be used together with the electron energy,  $\gamma_b$ , to estimate the wiggler  $K$  parameter, making one assumption about the local plasma density difference. The critical energy is given only by  $\gamma_b$  and the minimum radius of curvature,  $\rho_0$ , of the electron trajectories. This gives  $\rho_0 = 3hc\gamma_b^2 / (2E_c) \approx 1.37 \text{ cm}$  (ref. <sup>8</sup>), which yields  $K = \gamma_b \lambda_p / (2\pi\rho_0) \approx 9.1$ . Here, the used betatron wavelength,  $\lambda_p$ , corresponds to a density  $n_p = 2.5 \times 10^{17} \text{ cm}^{-3}$ , that is, 2.5% of the jet 2 peak density, suggesting a partially evacuated wake at the peak density of  $n_p = 1 \times 10^{19} \text{ cm}^{-3}$ . This density difference is close to the one obtained from the PIC simulations, and thus corroborates the result that the shock-bunch is located in a weak wake. A  $K$  parameter of 9, given 2 pC of charge and half a betatron cycle, gives  $1.9 \times 10^6$  photons at the average energy of  $\langle E \rangle \approx 0.3E_c$  (ref. <sup>8</sup>). The above density difference also suggests a reasonable betatron oscillation amplitude of  $\sim 6.8 \mu\text{m}$ , and density differences in the range  $n_p = 2.5\text{--}5 \times 10^{17} \text{ cm}^{-3}$  similarly yield reasonable photon numbers and betatron radii, but the resulting  $K$  parameter is not consistent with estimations of the X-ray divergence due to the fact that only a fraction of a betatron oscillation is performed in our case. Further details and discussion are provided in the Supplementary Information.

**PIC simulations.** PIC simulations were carried out using the fully relativistic and quasi-axisymmetric code CALDER-Circ<sup>35</sup>, in which three modes are used for the azimuthal Fourier decomposition of the fields and currents. The moving window following the laser pulse is composed of  $4,320 \times 300$  cells, with longitudinal and radial steps  $\Delta x = 0.125c/\omega_0$  and  $\Delta r = 2c/\omega_0$ , respectively, where  $c$  is the speed of light and  $\omega_0$  the laser frequency. The corresponding time step is  $\Delta t = 0.123\omega_0^{-1}$ , and a scheme reducing the numerical Cherenkov radiation<sup>52</sup> when solving the Maxwell equations is used. The density profile used in the simulation is shown in Fig. 4a: jet 1 consists of a fourth-order, 1.6-mm-wide (FWHM) super-Gaussian, with the maximum background electron density of  $n_p = 6.3 \times 10^{18} \text{ cm}^{-3}$ , and five times pre-ionized nitrogen ions with a number density of  $n_{\text{N}^{5+}} = 6.3 \times 10^{16} \text{ cm}^{-3}$ . The ionization of the K-shell of the nitrogen ions is modelled using the Ammosov–Delone–Krainov-based model of the code<sup>53</sup> and a neutralizing immobile ion background is used so that the plasma is initially neutral. Jet 2 consists of a 1.0-mm-wide (FWHM) Gaussian and is composed of pure electron species at a density of  $1.0 \times 10^{19} \text{ cm}^{-3}$ ; as  $a_0 \approx 0.5$ , N<sup>5+</sup> ionization is assumed throughout jet 2. Thirty-two macroparticles per cell are used for the electrons and two macroparticles per cell for the nitrogen ions.

In the simulations, a 0.9-J, 35-fs-long laser pulse is focused on a spot size of 14  $\mu\text{m}$  FWHM at the entrance of jet 1, resulting in a normalized vector potential of  $a_0 = 1.9$ . The laser is polarized horizontally, in the  $x$  direction.

Radiation results are post-processed from the trajectories of  $\sim 10^4$  representative electrons—achieving a maximum energy above 30 MeV—that are recorded during the PIC simulations. The radiated energy  $d^2W/d\omega d\Omega$  per frequency unit  $d\omega$  and per solid angle unit  $d\Omega$  in the direction  $\mathbf{n}$  is calculated using<sup>54</sup>:



$$\frac{d^2 W}{d\omega d\Omega} = \frac{e^2}{16\pi^3 \epsilon_0 c} \left| \int_{-\infty}^{\infty} e^{i\omega(t - \frac{\mathbf{n} \cdot \mathbf{r}(t)}{c})} \frac{\mathbf{n} \times [(\mathbf{n} - \boldsymbol{\beta}(t)) \times \dot{\boldsymbol{\beta}}(t)]}{(1 - \boldsymbol{\beta}(t) \cdot \mathbf{n})^2} dt \right|^2,$$

for a particle whose trajectory, speed and acceleration are respectively  $\mathbf{r}(t)$ ,  $\boldsymbol{\beta}(t) = \mathbf{v}(t)/c$  and  $\dot{\boldsymbol{\beta}}(t) = d\boldsymbol{\beta}(t)/dt$ , and where  $e$  is the unit charge and  $\epsilon_0$  the vacuum permittivity.  $d^2 W/d\omega d\Omega$  is then integrated over an interval of 3–15 keV to obtain the X-ray divergences shown in Fig. 4d.

**Semi-analytical model.** As stated in the main text, the propagation of the beam envelope  $\beta$  function is governed by equation (1).  $\beta$  relates to the r.m.s. beam size as  $\sigma = \sqrt{\beta \epsilon_n / (\beta_b \gamma_b)}$ , where  $\epsilon_n$  is the normalized transverse emittance (invariant up to  $\sim 1$  cm of propagation) of the beam and  $\beta_b = v_b/c \approx 1$  is the normalized electron velocity. The behaviour of  $\beta$  is governed by  $\kappa$ , which is the normalized, linear focusing strength, which can be retrieved from the local forces on the electrons inside the wake, as described in the Supplementary Information. Most crucially,  $\kappa$  depends on the local plasma density and wake amplitude and phase, which vary significantly during propagation. Here, equation (13) in ref. 22 (Supplementary equation (6)) is used to obtain the transverse force in a linear laser-wake, inside which a dense electron beam drives a second wake, which is then used to evaluate  $\kappa$  at every step in the numerical solver. The chosen solver is based on an explicit Runge–Kutta (4,5) scheme. The model parameters that are not adapted from the experimental results are estimated using nonlinear analytic theory<sup>55</sup>, and the main parameters that are varied to fit the model to the experimental data are the longitudinal laser–electron beam separation,  $\xi_{\text{laser}}$ , and the distance behind the driver beam head,  $\xi_b$ . The estimated parameters are the laser pulse duration, energy and radius (assuming a waist at the jet 1 exit).

To obtain the best agreement with experiment, particularly for small jet separations, an addition to the model of charge ‘loss’ in the ionization-bunch is also made. Loss, in this sense, means that the charge no longer contributes to the wake excitation, which influences the shock-bunch. This is observed in the experiment for the ionization-bunch head (at  $\sim 120$  MeV) (Fig. 1b–d). This charge loss varies with jet separation, with the highest loss occurring for smaller separations, as also reported in ref. 31, and is therefore expected to depend both on the density of the ionization-bunch and the plasma in jet 2. The assumption is made that the loss of charge per unit travelled distance,  $dQ/ds$ , is proportional to the normalized beam density,  $\tilde{n}_b$  (similar to ref. 56), that is

$$\frac{dQ}{ds} = C \cdot \tilde{n}_b = C \cdot \frac{n_b}{n_p} k_p^3, \quad (2)$$

where  $C$  is a constant used for fitting. The value of  $C$  was found to be around  $5 \times 10^{-25} \text{ C m}^2$  when fitting for an appropriate charge loss in the ionization-bunch head at the given jet separations. The ionization-bunch propagation is assumed not to be affected by this, so the charge loss is implemented after calculation of the ionization-bunch propagation and before the shock-bunch propagation. For more details, see Supplementary Information.

The radiated power emitted by the electrons is calculated for this model using

$$P_{\text{rad}}(s) = \frac{Q_b e^3 \gamma_b^2}{6\pi m_e^2 \epsilon_0 c} g_q^2(s) (\sigma_x^2(s) + \sigma_y^2(s)), \quad (3)$$

and the critical energy is calculated with

$$E_c = \frac{3 \hbar e}{2 m_e} \gamma_b^2 g_q(s) \sqrt{\sigma_x^2(s) + \sigma_y^2(s)}. \quad (4)$$

See Supplementary Information for derivations. The radiated power was verified by tracking a sample of 1,000 randomized electrons through the same focusing gradients and calculating the radiation with the same method as for the PIC simulations. The total radiated energy is calculated by integrating this equation over jet 2. The effective X-ray divergence for radiation above 4 keV (as detected in the experiment) is estimated by calculating  $\theta_{\text{eff}} = \sqrt{P_{\text{rad}} \theta_{\text{dl}}^2 / P_{\text{rad}}}$ , with  $\theta = \sqrt{\sigma_y^2 + (\theta_0/3.3)^2} = \sqrt{\sigma_y^2 + 1/(3.3\gamma_b)^2}$ , where  $\theta_0/3.3$  is the r.m.s. of the energy-averaged single-electron radiation distribution above 4 keV (see the

Supplementary Information for a digression on this).

As  $\sigma_y$  was the parameter compared to the measurement and  $\sigma_x$  was not measured, the influence of DLA was thus not quantified. The distribution along  $x$  was therefore simply estimated by increasing the  $x$  emittance by a factor of 10, using the same Twiss functions otherwise. This is an approximation (see Supplementary Information for further discussion).

Similar to  $\beta$ , the parameter  $\gamma$  is used to describe the electron beam divergence as  $\sigma_y = \sqrt{\gamma \epsilon_y}$ . Together with the above equation for  $\theta$ , a simple guiding condition can be found (Supplementary Information) for how much to expand the beam size so as not to limit the X-ray divergence with the electron-beam transverse properties. The condition is  $\sigma_y \gg \epsilon_{ny} \gamma$ , where  $\gamma$  is a numeric factor that depends, for example, on part of the detected X-ray spectrum ( $\gamma = 3.3$  above). If this condition is met, the electron beam divergence does not increase the X-ray divergence and only the single-electron emission, and thus  $\gamma_b$ , will determine it. Using the Gaussian fit to the azimuthally averaged divergence distribution

(Supplementary Information),  $\gamma = 2.8$  and thus  $\gamma_b \gtrsim 850$  would yield a sub-1-mrad FWHM X-ray divergence for the full spectrum.

**Data treatment.** Because of double peaks and asymmetry in the spectrum (here denoted  $S(E)$ ) of many shock-bunches, the peak energy of these electrons is calculated as the ‘centre of mass’ (or centroid) within  $E_{\text{peak}} \pm 2 \times E_{\text{hw}}/2$ , that is

$$E_{\text{centroid}} = \frac{\int_{E_{\text{peak}} - 2E_{\text{hw}}/2}^{E_{\text{peak}} + 2E_{\text{hw}}/2} S(E) \cdot E dE}{\int_{E_{\text{peak}} - 2E_{\text{hw}}/2}^{E_{\text{peak}} + 2E_{\text{hw}}/2} S(E) dE},$$

where  $E_{\text{peak}}$  is the energy of the maximum of the spectrum over the whole shock-bunch and  $E_{\text{hw}}/2$  is the half-width at half-maximum of the upper and lower slopes of the maximum peak, respectively. To accommodate odd spectral shapes, the FWHM points are chosen as the outermost points where the signal value reaches below half of the maximum. The related metrics remaining energy fraction and remaining charge fraction<sup>31</sup> could not be evaluated in a meaningful way because of the additional low-energy charge that was observed with jet 2 on.

Once the bounds in energy of the peak are identified, the centroid divergence of the peak is calculated in a similar way, over the same range as the energy. The denominator in these integrals is simply the shock-bunch charge. The charge of the ionization-bunch is then calculated as the total beam charge (from 14 MeV, at the lower end cutoff, up to 260 MeV) minus the shock-bunch charge. The centroid energy of the ionization-bunch is also calculated in this way.

The electron spectrometer images in Fig. 1b are filtered using a  $3 \times 3$  pixel median filter, to reduce noise from bremsstrahlung on the camera chip. The resolution of the zoomed electron spectrometer images in Fig. 2a–c is doubled in both axes by linearly interpolating the images. The X-ray profile images in Fig. 3a,b are binned in a  $2 \times 2$  pixel grid, followed by a  $4 \times 4$  pixel median filter, to reduce noise and make the images clearer in print.

## Data availability

Data that support the plots within this paper and other findings of this study are available from the corresponding author upon reasonable request. Source data are provided with this paper.

## Code availability

The codes that support the findings of this study are available from the corresponding authors upon reasonable request.

## References

- Schmid, K. & Veisz, L. Supersonic gas jets for laser-plasma experiments. *Rev. Sci. Instrum.* **83**, 053304 (2012).
- Kurz, T. et al. Calibration and cross-laboratory implementation of scintillating screens for electron bunch charge determination. *Rev. Sci. Instrum.* **89**, 093303 (2018).
- Smith, S. W. *The Scientist & Engineer's Guide to Digital Signal Processing* 1st edn (Elsevier, 2002).
- Esarey, E., Shadwick, B. A., Catravas, P. & Leemans, W. P. Synchrotron radiation from electron beams in plasma-focusing channels. *Phys. Rev. E* **65**, 056505 (2002).
- Lehe, R., Lifschitz, A., Thaur, C., Malka, V. & Davoine, X. Numerical growth of emittance in simulations of laser-wakefield acceleration. *Phys. Rev. ST Accel. Beams* **16**, 021301 (2013).
- Nuter, R. et al. Field ionization model implemented in particle in cell code and applied to laser-accelerated carbon ions. *Phys. Plasmas* **18**, 033107 (2011).
- Jackson, J. D. *Classical Electrodynamics* 3rd edn (Wiley, 1999).
- Lu, W. et al. A nonlinear theory for multidimensional relativistic plasma wave wakefields. *Phys. Plasmas* **13**, 056709 (2006).
- Rosenzweig, J. B., Barov, N., Thompson, M. C. & Yoder, R. Energy loss of a high charge bunched electron beam in plasma: nonlinear plasma response and linear scaling. *AIP Conf. Proc.* **647**, 577–591 (2002).

## Acknowledgements

We thank D. Cardenas for his help and support. We acknowledge support from the Swedish Research Council (VR 2015-03749, 2019-04784), the Knut and Alice Wallenberg Foundation (KAW 2014.0170, 2018.0450 and 2019.0318), the European Research Council (ERC-2014-CoG 647121), Laserlab-Europe (EU-H2020 871124) and ARIES (EU-H2020 730871). L.V. acknowledges support from the Swedish Research Council (VR 2016-05409 and 2019-02376). H.E. acknowledges support from the US Department of Energy (DE-AC02-76SF00515). J.F. acknowledges support from the Swedish Research Council (VR 2016-03329). Simulations were performed on resources at C3SE and LUNARC, provided by the Swedish National Infrastructure for Computing (SNIC).

## Author contributions

J.B.S., D.G., L.V. and O.L. devised the experiment. J.B.S. and D.G. built the experimental set-up and performed the measurements assisted by I.G.G., H.E., K.S. and A.P. J.B.S.

analysed the electron data and constructed the semi-analytical model. D.G. and H.E. analysed the X-ray data. J.F. and H.E. performed and analysed the PIC simulations. O.L. supervised the work. J.B.S., D.G., J.F. and L.V. wrote the manuscript, with input and feedback from all authors.

### **Competing interests**

The authors declare no competing interests.